Cement & Concrete Composites 36 (2013) 71–77

Contents lists available at SciVerse ScienceDirect

Cement & Concrete Composites

journal homepage: www.elsevier.com/locate/cemconcomp

Density mapping of hardened cement paste using ptychographic X-ray computed tomography

Pavel Trtik [a,*], Ana Diaz [b], Manuel Guizar-Sicairos [b], Andreas Menzel [b], Oliver Bunk [b]

[a] Empa, Laboratory for Concrete and Construction Chemistry, Swiss Federal Institute for Materials Science and Technology, Dübendorf CH-8600, Switzerland
[b] Paul Scherrer Institut, Villigen PSI CH-5232, Switzerland

ARTICLE INFO

Article history:
Received 1 February 2012
Received in revised form 11 May 2012
Accepted 7 June 2012
Available online 16 June 2012

Keywords:
Hardened cement paste
Density
C–S–H
Calcium hydroxide
Image analysis
Phase retrieval
Computed tomography
Coherent diffractive imaging

ABSTRACT

Ptychographic X-ray computed tomography (PXCT) allows for a non-destructive, three-dimensional mapping of the electron density. Its quantitativeness combined with a resolution in the 100 nm range makes it a suitable tool for the assessment of densities of the individual phases in complex materials, such as hardened cement pastes. Here we present results of an experiment performed on a cylindrical sample of epoxy-impregnated hardened cement paste of about 30 μm in diameter. Two-dimensional cross sections of the three-dimensional electron density map show a microstructure that bears distinct similarity to that observed by back-scattered scanning electron microscopy. Domains of various residues of cement grains, calcium hydroxide, calcium carbonate, epoxy-resin impregnated calcium silicate hydrates, epoxy-resin impregnated porosity, and unimpregnated porosity are revealed and are manifested as distinguishable peaks in the histogram of the three-dimensional electron density map. On assumptions of (i) a priori knowledge of the chemical composition and (ii) the purity of the analysed regions, the mass densities of the above mentioned individual material phases are estimated. The potential of PXCT for the science of cement and concrete is discussed.

1. Introduction

The development of durable cementitious materials is one of the long-term goals of the science of cement and concrete [1], and therefore the information on the 3D distribution of the material phases, and hence the distribution of the mass density, within the microstructure of cementitious materials, is of significant interest. The mass density of the individual material phases is also important for modelling [2,3] of processes occurring in the cementitious materials, e.g., hydration, degradation, etc.

Many material phases occurring in cementitious materials are crystalline, and therefore their theoretical mass densities can be calculated based on the knowledge of their crystal structure. However, a number of hydrated cementitious phases, including the most abundant phase of ordinary Portland cement pastes – calcium silicate hydrates C–S–H, exhibit only short-range order of crystallinity. To reveal the information on their atomic scale structure and the extent of their naturally occurring nanoporosity that intrinsically affects the density, hence physical properties, is not trivial. For such material phases advanced methods must be used to retrieve their mass density. Allen et al. [4] derived the composition and density of basic building blocks of C–S–H from small-angle neutron and X-ray scattering. Skinner et al. [5] reported the composition of the building blocks of C–S–H using a pair distribution function analysis of X-ray diffraction data. These experiments were performed on bulk samples of model materials and therefore cannot provide information on the density distribution on the micro- and nanoscale. Neither can the information on the density of materials occurring in real cementitious systems be provided.

For a detailed understanding of real cementitious systems mass density information need to be determined with high spatial resolution. Techniques based on nanomechanical resonators [6] can be used to assess the densities of very small objects, such as single cells and even single nanoparticles [7], but their use for the study of cementitious materials is limited, because it is intrinsically difficult to physically separate individual phases from the bulk.

The capability for high spatial resolution imaging is a well-known property of electron and X-ray microscopy. Electron microscopy has been used for the quantitative assessment of cementitious materials for decades [8,9]. The back-scattered electron (BSE) contrast is linked to the composition of different phases, and the back-scattered electron coefficient of a material phase can be derived from the average atomic number. However, the mass density cannot be retrieved quantitatively, neither from 2D BSE images nor from its 3D variant – focussed ion beam nanotomography [10]. Full-field X-ray tomography currently achieves about 50 nm resolution [11]. In absorption mode, it reveals the distribution of the linear attenuation coefficient. However, X-ray absorption contrast does not provide quantitative measurements of the electron density

* Corresponding author.
E-mail address: ptrtik@gmail.com (P. Trtik).

0958-9465/$ - see front matter © 2012 Elsevier Ltd. All rights reserved.
http://dx.doi.org/10.1016/j.cemconcomp.2012.06.001

[12] unless measurements are performed at different X-ray energies [13]. X-ray Zernike phase contrast [14] is only quantitative for objects with negligible absorption and a small phase shift [15]. On the other hand, tomography using coherent X-ray imaging methods, such as ptychography [16] and holography [17], can provide quantitative 3D reconstructions of the electron density of the sample.

In this paper, we report the results of the recently established ptychographic X-ray computed tomography (PXCT) on a sample of epoxy resin impregnated hardened cement paste. The objective of the reported experiment was to (i) reveal the microstructure of epoxy impregnated hardened cement paste, (ii) quantify the electron density of material phases, and (iii) derive the mass density of the material phases based on an estimation of their chemical composition.

1.1. Ptychographic X-ray computed tomography (PXCT)

In X-ray ptychography [18,19] a pinhole or a focusing element is used to define a spatially confined coherent illumination onto the sample. Diffraction patterns are recorded in the far field for many overlapping illumination regions of the specimen. The sample is mounted on a three-dimensional translation stage with nanometre resolution in all directions (see Fig. 1a). The redundancy in the data stemming from the illumination of overlapping regions allows for retrieval of the complex transmission function of the sample using iterative reconstruction algorithms, providing information about both the amplitude and the phase shift contrasts with a spatial resolution that is finer than the scanning step and the size of the illumination.

The phase shift can be defined as the shift of the incident wavefield phase $\phi(x,y)$ as it passes through the object and can be expressed as

$$\phi(x,y) = -\frac{2\pi}{\lambda}\int \delta(\mathrm{r})dz, \tag{1}$$

where $\delta(\mathrm{r})$ is the difference from unity of the real part of the refractive index within the object, λ is the wavelength of the incoming radiation, and z is the propagation direction (see Fig. 1).

PXCT combines many ptychographic reconstructions at different incidence angles of the X-ray beam. A rotation stage positioned below the scanning stage is used to change the incidence angle of the beam onto the sample (see Fig. 1a). A phase projection, reconstructed using the algorithm described in [20], is shown in Fig. 1b.

Tomographic reconstruction from phase projections at different sample orientations provides the 3D distribution of the real part of the refractive index, $\delta(r)$, of the specimen on the nanoscale [16]. The 3D electron density distribution can be readily obtained by

$$n_e(\mathrm{r}) = \frac{2\pi\delta(\mathrm{r})}{r_0\lambda^2}, \tag{2}$$

where r_0 is the classical electron radius. The mass density can be derived from the electron density as,

$$\rho = \frac{n_e A}{N_A Z}, \tag{3}$$

where A is the molar mass of a compound, Z is the total number of electrons per mole in a compound, and N_A is Avogadro's number. Consequently, the knowledge of the chemical composition of the sample is required for the accurate measurement of the mass density.

Diaz et al. [21] recently investigated model objects composed of materials of known densities and validated that PXCT provides quantitatively correct results of the local mass density with the relative error as low as 0.8%. It needs to be stressed that the measurement of relative error strongly depends on the voxel size of the 3D density maps. In other words, the binning of reconstructions provides a trade-off between resolution and sensitivity. An uncertainty for density measurements of below 2.7% has been shown for voxel sizes of about 700 nm for a broad range of investigated material densities [21].

The current state-of-the-art of the technique allows for investigations of samples of several tens of microns in size with spatial resolution of about 100 nm and although the maximum thickness of the specimen is limited by an effective depth-of-field [20] and multiple scattering effects, thicknesses of up to 100 μm can be investigated without compromising the currently achievable resolution.

2. Experimental

2.1. Sample preparation

The sample preparation was similar to that reported in Trtik et al. [22]. In the first step, a 20 × 20 × 10 mm block of hardened cement paste ($w/c = 0.5$) was produced from white Portland cement (Aalborg white) that was cured in water for 21 days after demoulding.

Afterwards, the block was impregnated using a common methodology for the epoxy impregnation for back-scattered electron microscopy. Then, the sample was cut into four similar parts and two orthogonal surfaces of one of these parts were polished in such a way that a sharp 90° edge of material was created. A location on this edge that had originally resided well inside the block of material was selected arbitrarily. From this location, a cube-like object of about 40 μm side was machined using high current (18 nA) focussed ion beam (FIB) milling. Fig. 2a shows one of these cube-like objects still positioned at the sharp 90° edge. The object was then transferred onto the tip of a stainless steel holder using a micromanipulator and was fixed by means of a small droplet of UV-hardening glue (see Fig. 2b). In the next step, a cylindrical

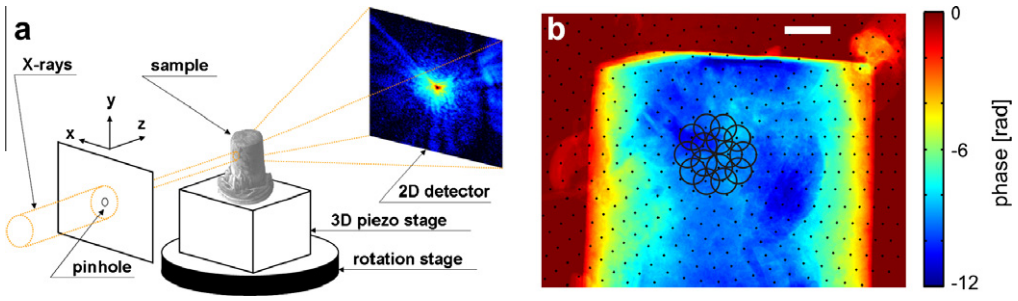

Fig. 1. (a) Sketch of the experimental setup for ptychographic X-ray computed tomography. At each incidence angle coherent diffraction patterns are recorded by a pixelated detector for a number of overlapping scanning positions, which allows the projected complex-valued transmission function to be reconstructed. (b) Example of a single reconstructed phase projection of the epoxy resin impregnated hardened cement paste sample. The black dots indicate the scanning positions at which diffraction patterns were recorded, and the black circles represent the approximate shape of the beam – shown for the first two shells of the circular scan only. The scale bar corresponds to 5 μm.

specimen of about 30 μm in diameter was micromachined from the cube-like object using high-current (18 nA) FIB milling. The top surface of the specimen was machined by means of low-current (300 pA) FIB milling.

2.2. PXCT test arrangement and data processing

The experiments were performed at the cSAXS beamline at the Swiss Light Source, Paul Scherrer Institut, Switzerland. The photon energy of the X-ray beam was 6.2 keV. A 2.5 μm pinhole, located 2.5 mm upstream of the sample, defined the coherent illumination onto the sample. Coherent diffraction patterns were acquired with a zero readout noise, single-photon counting detector [23] placed 7.2 m downstream of the sample. A He-flushed tube in between the sample and the detector was used to reduce X-ray scattering and absorption by air.

Each phase projection required 425 coherent diffraction patterns to cover the desired field of view. The patterns were acquired by scanning in concentric circular shells within a 40×30 μm area of interest. The first shell consisted of five scanning points equally spaced on a circumference of 3 μm in diameter. The radial step to each next shell equalled 1.5 μm and provided sufficient beam overlap (see Fig. 1b).

Three hundred and sixty phase projections were acquired at different incidence angles starting from 0° to 179.5° with steps of 0.5°. Having an acquisition time of a single diffraction pattern of 0.4 s, the total acquisition time of all 153,000 diffraction patterns was 17 h. With the time necessary for sample positioning, the experiment was completed within approximately 25.5 h.

The reconstructions of individual ptychographic scans were performed using the difference map algorithm described in Thibault et al. [24]. The pixel size of the phase projections equalled 43.6 nm. Thus-obtained phase projections were first post-processed in order to remove linear and global offsets in phase-shift [25]. For this, about 50 pixels wide regions of air around the sample were used. Later, the phase projections were unwrapped to allow the phase shift to be spanned over an extended range instead of the $(-\pi,\pi>$ range that is obtained from the original reconstructions. Also, the phase maps were mutually aligned with sub-pixel precision [25]. The phase maps from all the incidence angles were used in a filtered back projection tomographic reconstruction resulting in the 3D refractive index map of the sample. The corresponding 3D electron density map can be derived using Eq. (2).

3. Results and discussion

The procedure described in Section 2 yielded the 3D electron density map of epoxy resin impregnated hardened cement paste of $896 \times 896 \times 581$ voxels in size. A subset predominantly leaving out the regions corresponding to air in the sample vicinity was cropped out from the original dataset. The size of this further-analysed dataset was $720 \times 720 \times 420$ voxels corresponding to a volume of about $31.4 \times 31.4 \times 18.3$ μm^3. A horizontal cross section of the 3D electron density map that clearly reveals the inner microstructure of the sample is shown in Fig. 3a, and the histogram of the entire $720 \times 720 \times 420$ dataset is shown in Fig. 3b. We note that the microstructure of hardened cement paste revealed by PXCT bears distinct resemblance to that revealed by back-scattered electron microscopy, as further discussed in Section 4.

The histogram of the unbinned electron density data suggests a number of different material phases. In order to better distinguish different material phases from the histogram, the data were binned by averaging the electron density in regions of $6 \times 6 \times 6$ voxels, thus reducing both the spatial resolution of the dataset (see Fig. 4a) and the spread of the density distribution of the individual material phases (see Fig. 4b).

The histogram of the binned dataset (Fig. 4b) was used to provide the thresholds for the material phase segmentation. Six different material phases were distinguished and were identified as follows: unimpregnated/'partially impregnated' porosity, epoxy-impregnated porosity, other hydrates (predominantly epoxy-impregnated calcium–silicate–hydrates), calcium hydroxide, calcium carbonate, and unhydrated/'partially-hydrated' cement residues. The surface renderings of the individual identified material phases are shown in Fig. 5.

Thanks to its quantitativeness [21], PXCT allows measurements of the electron densities of the individual phases. Using a priori knowledge of the chemical composition the mass densities of the individual phases can be derived. The measured electron densities, the estimated chemical composition and the derived mass densities are summarised in Table 1.

Due to the non-representative sample size [26], we refrain from the quantitative analysis of the morphology of the revealed material phases. Instead, we focus on the discussion of the quantitative results of the obtained mass densities of the individual material phases.

3.1. Porosity

PXCT results show that most of the resolvable pore space has been filled by the epoxy resin (see Fig. 5b), while only a small portion of the resolvable pore space remained unimpregnated or only partially impregnated with epoxy resin (see Fig. 5a). The measured mass density for the epoxy resin impregnated pore space ($\rho_{\text{epoxy resin}} = 1.14 \pm 0.10$ g/cm^3) matches exactly with the density that was measured for the bulk hardened epoxy resin by simple mass and volume measurements for a sample size of about several cm^3.

3.2. Other hydrated phases

As mentioned above, knowledge of the chemical composition of a material phase is required for the accurate calculation of its mass

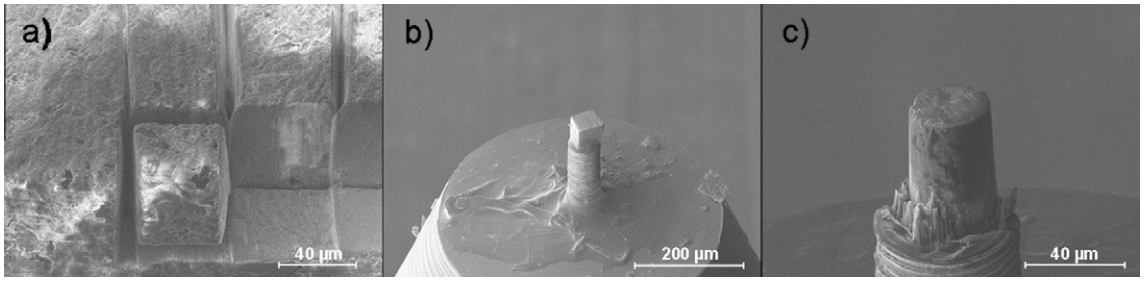

Fig. 2. (a) A view of the 90° sharp edge of epoxy-impregnated hardened cement paste from which a cube-like object was machined using focussed ion beam (FIB) milling. One of the objects is visible in about the centre of the image with the recesses remaining on the right after other similar objects were extracted. (b) The cube-like object positioned on the top of a stainless steel sample holder and (c) the final specimen produced by micromachining of the object in Fig. 2b into cylindrical shape using FIB milling.

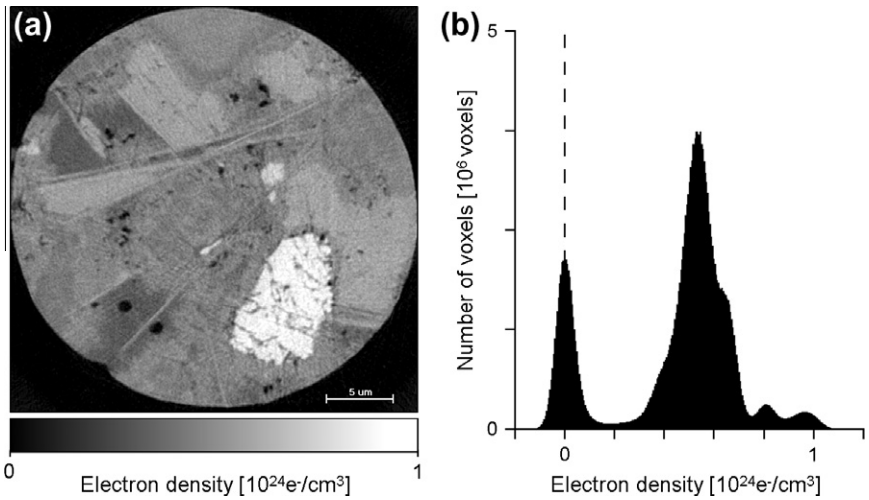

Fig. 3. (a) Horizontal cross-section of the PXCT dataset (no binning, pixel size 43.6 nm). (b) Histogram of the electron density for 720 × 720 × 420 voxels. The dashed line marks the position of the *y*-axis at the zero electron density.

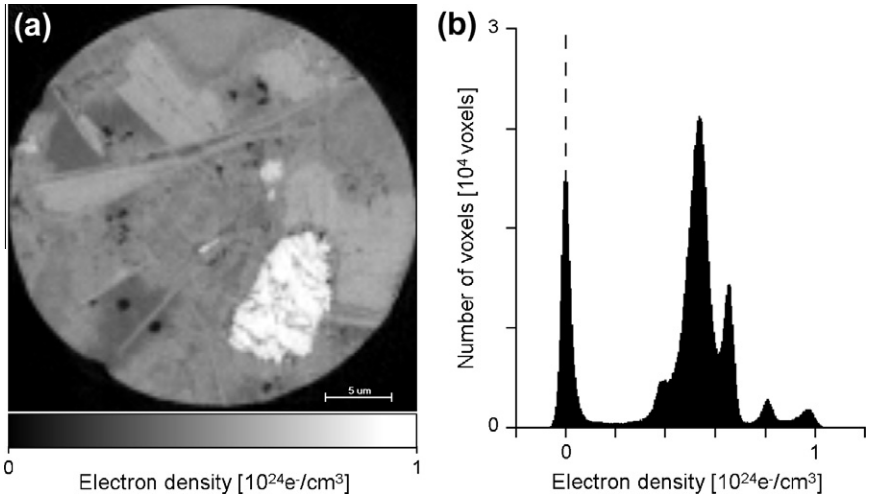

Fig. 4. (a) Horizontal cross section of the PXCT dataset (after 6 × 6 × 6 binning, pixel size 261.6 nm). (b) Histogram of the electron density for 120 × 120 × 70 binned voxels. The dashed line marks the position of the zero electron density.

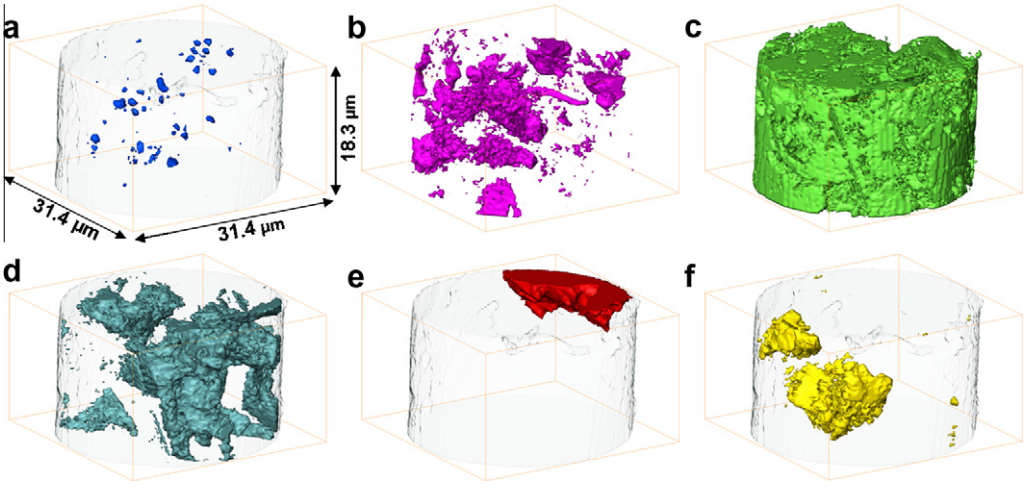

Fig. 5. Surface renderings showing the identified individual material phases. (a) Unimpregnated/'partially impregnated' porosity, (b) epoxy-impregnated porosity, (c) other hydrates (predominantly epoxy-impregnated calcium–silicate–hydrates), (d) calcium hydroxide, (e) calcium carbonate, (f) unhydrated/'partially hydrated' clinker residues.

Table 1
Measured electron densities, estimated chemical composition, and estimated mass density of the identified material phases. The standard deviation of the electron density measurement is based on the binned dataset for the entire regions of the identified phases (as shown in Fig. 5). The value X represents the unknown and likely spatially variable ratio between epoxy resin and nanoscale C–S–H particles that may theoretically assume values between 0 and 1, though a value based on a realistic particle packing (see Ref. [27]) is expected.

Material phase	Measured electron density ($10^{23}e^-/cm^3$)	Estimated chemical composition	Estimated mass density (g/cm^3)
Unimpregnated/partially impregnated porosity	0.67 ± 0.22	N/A	N/A
Epoxy-resin impregnated porosity	3.70 ± 0.32	$C_{86}H_{126}O_{18}Cl_3N_2$	1.14 ± 0.10
Other hydrates (predominantly epoxy-resin impregnated calcium–silicate–hydrates)	5.27 ± 0.36	$(1-X)(C_{86}H_{126}O_{18}Cl_3N_2)+X(CaO)_{1.7}(SiO_2)(H_2O)_{1.8}$	$(1.63 + 0.09 X) \pm (0.11 + 0.01 X)$
Calcium hydroxide	6.56 ± 0.18	$Ca(OH)_2$	2.12 ± 0.06
Calcium carbonate	8.04 ± 0.20	$CaCO_3$	2.67 ± 0.07
Unhydrated/partially hydrated clinker residues	9.65 ± 0.31	Ca_2SiO_4	3.21 ± 0.11

density. Based on the composition of the white cement used, this phase is to be predominantly composed of epoxy resin impregnated calcium silicate hydrates, although minor quantities of ettringite (expected density 1.78 g/cm^3) will also be present. The density of C–S–H is very much dependent on the amount of water that is incorporated in its structure as chemically bound water, adsorbed water, or water contained in nanopores. Therefore, to express the chemical composition of epoxy impregnated calcium silicate hydrate is intrinsically difficult, even based on the assumption that C–S–H is fully impregnated with epoxy resin and that only chemically bound water would remain in the sample. On the other hand, it is worth noting here that apart from hydrogen all the other major elements to be found both in the epoxy resin and in the C–S–H exhibit a ratio of the molar mass to the number of electrons per atom (A/Z) very close to 2 g. Consequently, the uncertainty in the estimate of the mass density of this phase based on the measurement of the electron density is rather low. As shown in Table 1, the average mass density of this phase may vary between 1.63 and 1.72 g/cm^3 only, in spite of the fact that the lower bound assumes the chemical composition of the pure epoxy resin, while the upper bound is based on the proposed composition of the pure nanoscale C–S–H particles [4]. The above-mentioned density interval is not far from the density of 1.83 g/cm^3 that was derived from the colloidal model of C–S–H by Jennings [27] for the considered composition of $C_{1.7}SH_5$ and particle packing $\eta = 0.59$. Since other mechanisms, such as carbonation-induced decalcification of C–S–H [28] and an incomplete epoxy resin impregnation of the porosity below the spatial resolution limit of PXCT dataset, might be responsible for this small discrepancy, we propose that PXCT is suited for the determination of the density of C–S–H phases within hardened cement pastes. Future PXCT investigations on epoxy unimpregnated hardened cement pastes (see Section 5) may experimentally reveal the density range of C–S–H.

3.3. Calcium hydroxide

Calcium hydroxide is present in the structure of Portland cement paste in a number of forms with the sizes of its structural features spanning several orders of magnitude. Calcium hydroxide may be present as 1–10 nm crystals within C–S–H, as thin elongated platelets tens to hundreds of nanometres in thickness and as large agglomerates of high geometrical complexity tens of micrometres in size [29].

As shown in Figs. 3a and 5d, PXCT revealed both the elongated platelets of calcium hydroxide and the complex calcium hydroxide agglomerates of several micrometres in size occurring in the sample. The complexity of calcium hydroxide domain could have hitherto been revealed with sub-micron spatial resolution in 3D only by modified focussed ion beam nanotomography [30]. Since the regions of calcium hydroxide may be considered as obstacles that may direct the liquid flow in the porous medium [31], the knowledge of spatial distribution of calcium hydroxide in the microstructure of hardened cement paste on a representative volume element (RVE) [32] would be very valuable as an input for simulations of transport properties of hardened cement paste [1,33].

Regarding the observed mass density, the phase identified as calcium hydroxide exhibited a mass density of 2.12 ± 0.06 g/cm^3, which is about 5.7% lower than the expected value for portlandite ($\rho_{portlandite} = 2.251$ g/cm^3) [34]. As in the case of the epoxy impregnated C–S–H, the lower-than-expected density might be attributed to porosity below the spatial resolution and to the partial decalcification of the calcium hydroxide due to the carbonation. Also, the regions of AFm phases – of the expected densities between about 1.98 and 2.17 g/cm^3 [34] – expected to be present as a minor volume phases might be included in the segmented map of calcium hydroxide.

3.4. Calcium carbonate

As shown in Fig. 5e, one relatively large particle of calcium carbonate positioned close to the upper surface of the sample was present in the investigated paste. The measured mass density of the region identified as calcium carbonate ($\rho_{calcium\ carbonate} = 2.67 \pm 0.07$ g/cm^3) matches well with the expected value of density of calcite ($\rho_{calcite} = 2.710$ g/cm^3) [34]. The identification of this phase was later confirmed by means of post-PXCT energy dispersive X-ray spectroscopy (EDX). This result confirms that PXCT provides quantitatively correct density maps over a broad spectrum of the material mass densities.

3.5. Residues of cement particles

As shown in Figs. 3a and 5f, the sample contained two relatively large and several small residues of cement particles. The large residues show striations similar to those observed by Scrivener [9], thus suggesting the residues were originally composed of belite. The mass density obtained by PXCT within the region of these residues was $\rho_{residues} = 3.21 \pm 0.11$ g/cm^3, which is about 3.5% lower than ($\rho_{belite} = 3.326$ g/cm^3) reported in the literature for belite [34]. This lower value can be explained by the occurrence of the calcium-leached zones in the residues [35].

3.6. Consideration of the absorbed dose

Even though PXCT is a non-destructive technique, the induced radiation damage should be considered. Based on the estimate of the sample composition and the experimental arrangement, the total absorbed dose imparted to the sample was estimated to be about 2.0×10^6 Gy over the time necessary for the image acquisition. The absorbed dose is dependent on the composition of the

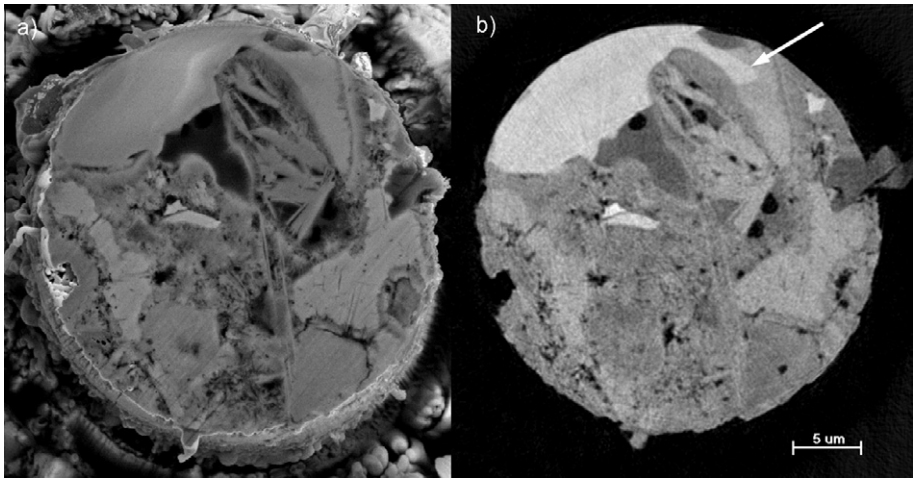

Fig. 6. Comparison of the post-PXCT back-scattered electron microscopy on the sample sectioned post-PXCT by focussed ion beam milling (a) with the approximately corresponding cross-section from the PXCT 3D density map (b). The arrow in Fig. 6b points at the apparent carbonation front within the originally calcium hydroxide domain.

sample, and therefore it will differ locally within the microstructure. No radiation-induced damage was observed during the experiment on the length scale accessible by PXCT.

4. Comparison of PXCT results with electron microscopy

A post-PXCT sample sectioning by means of a low-current FIB milling allowed for electron microscopy investigation. The back-scattered electron image at an accelerating voltage of 10 keV is shown in Fig. 6a, while the approximately corresponding PXCT-based density map is shown in Fig. 6b. For the latter an oblique slice was taken from the reconstructed tomographic dataset.

Even though the images show great similarities, some differences are apparent. First of all, it needs to be stressed that some of these differences are fundamentally linked with the non-planarity of the FIB-milled section. Atomic force microscopy images of a similarly prepared surface reported by Trtik et al. [22] indicate that the roughness of the surface produced in this way is likely larger than the voxel size of PXCT dataset. This incongruence prevents a reasonable application of a cluster analysis of the two images and imposes an interesting problem to be solved for any future comparison of the datasets based on X-ray and FIB nanotomography of the same sample.

Nevertheless, at least one apparent difference in the images cannot be attributed to the described incongruence. The arrow in Fig. 6b points at the boundary between calcium carbonate and calcium hydroxide domains within a likely originally calcium hydroxide region. The disappearance of the contrast within the particle in the post-PXCT BSE image suggests continuation of carbonation of this region. Hence, it provides an indication that a partial decalcification due to carbonation might have been partially responsible for the lower than expected values of the mass densities observed by PXCT for the calcium hydroxide and the epoxy-impregnated C–S–H phases.

5. Potential of PXCT for science of cement and concrete

Summarising the enhancing and limiting aspects of PXCT, we note:

- PXCT is a non-destructive imaging technique that delivers quantitative 3D maps of the electron density with high spatial resolution.
- The spatial resolution is currently limited by mechanical instabilities of the experimental setup. The resolving power is expected to improve below 100 nm in the near future.
- During the acquisition the sample is not required to be in vacuum.
- Obtaining the correct mass density from the electron density measured by this technique requires a priori knowledge of the chemical composition of the sample. It is foreseen that (at least for some sample types) a reasonable approximation of such information can be retrieved a posteriori using 3D FIB/EDX nanotomography [36] or by PXCT measurement performed at different X-ray energies.

PXCT may have some future potential for the science of cement and concrete [37]. It may prove very useful to shed some light in research questions in which electron microscopy techniques (both standard BSE imaging and FIB nanotomography) fail either due to the necessity to expose the sample to vacuum, their two-dimensionality, or the limited sample size.

Having 3D images of material microstructure based on reliable quantitative measurements of electron densities might be particularly useful for material phases that are intrinsically hard to be extracted from the bulk material without damage and whose mass densities cannot be easily derived by other methods. We foresee that future experiments performed on saturated samples encapsulated in microcapillaries will provide reliable measurement of densities of various hydrated phases, such as various forms of C–S–H, geopolymers [12], and other types of gels [38], etc. Such information will serve as valuable information for the thermodynamic modelling of cement hydration.

Since PXCT is non-destructive, further measurements can be done on the identical sample, either to investigate processes, such as the cement prehydration [39] and the early hydration [40], or to perform complementary studies, such as EDX in order to determine the chemical composition. Also, it is foreseen that the density of individual hydrated phases occurring within hardened cement pastes can be investigated in situ at different relative humidities, thus providing quantitative data for the (dis-)validation of structural models of complex materials [27], such as C–S–H. The hitherto limited temporal resolution might be alleviated by the application of smarter tomographic acquisition strategies [41]. For investigation of even faster processes, the PXCT of samples in cryogenic conditions [42] may be used as a possible though experimentally sophisticated alternative.

With hard X-rays assuring high penetration power, PXCT may also be used for investigations of cement pastes in sizes approaching those of the representative volume elements (RVE). The size of the RVE of hardened cement pastes is generally considered to be about $100 \times 100 \times 100\ \mu m^3$. Note however that the size of the RVE depends not only on the material microstructure but also on the particular investigated material property [43]. We believe that – with planned hardware improvements – the measurement of such a representative volume with resolution at or beyond 100 nm shall be feasible in the near future.

6. Conclusions

One sample of epoxy resin impregnated hardened cement paste was investigated by ptychographic X-ray computed tomography. The 3D maps of six individual material phases were successfully segmented from each other based on the quantitative determination of the electron density. To our knowledge, it is the first time that 3D maps of the individual material phases were revealed non-destructively with about 100 nm spatial resolution while simultaneously determining quantitatively the electron density of the identified phases and, thus, providing a basis for an accurate estimation of their mass densities. The derived mass densities of the individual phases matched well with the expected mass densities values. The technique is a useful tool for the quantitative investigations of cementitious and other nanostructured materials.

Acknowledgments

The authors would like to acknowledge Luigi Brunetti and Boris Ingold (both EMPA) for the assistance with the sample preparation and measurement of bulk density of epoxy resin. We gladly acknowledge that the FIB sample preparation was performed at EMPA, Electronics/Metrology/Reliability Laboratory. We thank Michael Stiefel for the assistance with post-PXCT FIB milling of the sample and acknowledge Xavier Donath's (PSI) technical assistance at the cSAXS beamline. We also thank Barbara Lothenbach and Beat Münch (both EMPA) for the critical reading of the manuscript.

References

[1] Leemann A, Loser R, Trtik P, Münch B. Optimierung der Permeanilität von Mörtel basierend auf 3D-Porenstrukturanalyse, Project report, cemsuisse-Projekt 200701; 2010.
[2] Lothenbach B, Winnefeld F. Thermodynamic modelling of the hydration of Portland cement. Cem Concr Res 2006;36(2):209–26.
[3] Lothenbach B, Damidot D, Matschei T, Marchand J. Thermodynamic modelling: state of knowledge and challenges. Adv Cem Res 2010;22(4):211–23.
[4] Allen AJ, Thomas JJ, Jennings HM. Composition and density of nanoscale calcium–silicate–hydrate in cement. Nat Mater 2007;6(4):311–6.
[5] Skinner LB, e SR, Benmore CJ, Wenk HR, Monteiro PJM. Nanostructure of calcium silicate hydrates in cements. Phys Rev Lett 2010;104(19):195502.
[6] Burg TP, Godin M, Knudsen SM, Shen W, Carlson G, Foster JS, et al. Weighing of biomolecules, single cells and single nanoparticles in fluid. Nature 2007;446(7139):1066–9.
[7] Grover WH, Bryan AK, Diez-Silva M, Suresh S, Higgins JM, Manalis SR. Measuring single-cell density. Proc Natl Acad Sci USA 2011;108(27):10992–6.
[8] Struble L, Stutzman P. Epoxy impregnation of hardened cement for microstructural characterization. J Mater Sci Lett 1989;8(6):632–4.
[9] Scrivener KL. Backscattered electron imaging of cementitious microstructures: understanding and quantification. Cem Concr Compos 2004;26(8):935–45.
[10] Holzer L, Indutnyi F, Gasser P, Munch B, Wegmann M. Three-dimensional analysis of porous $BaTiO_3$ ceramics using FIB nanotomography. J Microsc (Oxf) 2004;216(1):84–95.
[11] Le Gros MA, McDermott G, Larabell CA. X-ray tomography of whole cells. Curr Opin Struct Biol 2005;15(5):593–600.
[12] Provis JL, Rose V, Winarski RP, van Deventer JSJ. Hard X-ray nanotomography of amorphous aluminosilicate cements. Scr Mater 2011;65(4):316–9.
[13] Tsunoo T, Torikoshi M, Sasaki M, Endo M, Yagi N, Uesugi K. Distribution of electron density using dual-energy X-ray CT. IEEE Trans Nucl Sci 2003;50(5):1678–82.
[14] Stampanoni M, Mokso R, Marone F, Vila-Comamala J, Gorelick S, Trtik P, et al. Phase-contrast tomography at the nanoscale using hard X-rays. Phys Rev B 2010;81(14):140105.
[15] Trtik P, Soos M, Münch B, Lamprou A, Mokso R, Stampanoni M. Langmuir 2011;27(21):12788–91.
[16] Dierolf M, Menzel A, Thibault P, Schneider P, Kewish CM, Wepf R, et al. Ptychographic X-ray computed tomography at the nanoscale. Nature 2010;467(7314):436.
[17] Requena G, Cloetens P, Altendorfer W, Poletti C, Tolnai D, Warchomicka F, et al. Sub-micrometer synchrotron tomography of multiphase metals using Kirkpatrick–Baez optics. Scr Mater 2009;61(7):760–3.
[18] Faulkner HML, Rodenburg JM. Movable aperture lensless transmission microscopy: a novel phase retrieval algorithm. Phys Rev Lett 2004;93(2):023903.
[19] Rodenburg JM, Hurst AC, Cullis AG, Dobson BR, Pfeiffer F, Bunk O, et al. Hard-X-ray lensless imaging of extended objects. Phys Rev Lett 2007;98(3):034801.
[20] Thibault P, Dierolf M, Menzel A, Bunk O, David C, Pfeiffer F. High-resolution scanning X-ray diffraction microscopy. Science 2008;321(5887):379–82.
[21] Diaz A, Trtik P, Guizar-Sicairos M, Menzel A, Thibault P, Bunk O. Quantitative X-ray phase. Phys Rev B 2012;85:020104 (R).
[22] Trtik P, Kaufmann J, Volz U. On the use of peak-force tapping atomic force microscopy for quantification of the local elastic modulus in hardened cement paste. Cem Concr Res 2012;42(1):215–21.
[23] Kraft P, Bergamaschi A, Bronnimann C, Dinapoli R, Eikenberry EF, Graafsma H, et al. Characterization and calibration of PILATUS detectors. IEEE Trans Nucl Sci 2009;56(3):758–64.
[24] Thibault P, Dierolf M, Bunk O, Menzel A, Pfeiffer F. Probe retrieval in ptychographic coherent diffractive imaging. Ultramicroscopy 2009;109(4):338–43.
[25] Guizar-Sicairos M, Diaz A, Holler M, Lucas MS, Menzel A, Wepf RA, et al. Phase tomography from X-ray coherent diffractive imaging projections. Opt Express 2011;19(22):21345–57.
[26] Arns CH, Knackstedt MA, Mecke K. 3D structural analysis: sensitivity of Minkowski functionals. J Microsc 2010;240(3):181–96.
[27] Jennings HM. Refinements to colloid model of C–S–H in cement: CM-II. Cem Concr Res 2008;38(3):275–89.
[28] Papadakis VG, Vayenas CG, Fardis MN. Fundamental modeling and experimental investigation of concrete carbonation. ACI Mater J 1991;88(4):363–73.
[29] Material Science of Concrete. In: Skalny J, Gebauer J, Odler I, editors. Special volume: calcium hydroxide in concrete. Westerville (USA): The American Ceramic Society; 2001.
[30] Trtik P, Munch B, Gasser P, Leemann A, Loser R, Wepf R, et al. Focussed ion beam nanotomography reveals the 3D morphology of different solid phases in hardened cement pastes. J Microsc 2010;241(3):234–42.
[31] Bentz DP. Cement hydration: building bridges and dams at the microstructure level. Mater Struct 2007;40(4):397–404.
[32] Øren PE, Bakke S. Process based reconstruction of sandstones and prediction of transport properties. Transp Porous Media 2002;46(2–3):311–47.
[33] Promentilla MAB, Sugiyama T, Hitomi T, Takeda N. Quantification of tortuosity in hardened cement pastes using synchrotron-based X-ray computed microtomography. Cem Concr Res 2009;39(6):548–57.
[34] Balonis M, Glasser FP. The density of cement phases. Cem Concr Res 2009;39(9):733–9.
[35] Schweitzer JS, Livingston RA, Rolfs C, Becker HW, Kubsky S. Ion beam analysis of the hydration of tricalcium silicate. Nucl Instrum Methods Phys Res Sect B-Beam Interact Mater Atoms 2003;207(1):80–4.
[36] Schaffer M, Wagner J, Schaffer B, Schmied M, Mulders H. Automated three-dimensional X-ray analysis using a dual-beam FIB. Ultramicroscopy 2007;107(8):587–97.
[37] Nanocem: Nanoscale Research on Cement and Concrete. www.nanocem.org.
[38] Kurtis KE, Monteiro PJM, Brown JT, Meyer-Ilse W. Investigation of alkali-silica reaction by transmission soft X-ray microscopy. X-ray Microsc Proc Melville USA Am Inst Phys 2000;507:213–8.
[39] Winnefeld F. Influence of cement ageing and addition time on the performance of superplasticizers. ZKG Int 2008;61(11):68–77.
[40] Juilland P, Gallucci E, Flatt R, Scrivener K. Dissolution theory applied to the induction period in alite hydration. Cem Concr Res 2010;40(6):831–44.
[41] Kaestner A, Münch B, Trtik P, Butler L. Spatiotemporal computed tomography of dynamic processes. Optical Eng 2011;50(12):123201.
[42] Trtik P, et al. 2011;Unpublished data.
[43] Kanit T, Forest S, Galliet I, Mounoury V, Jeulin D. Determination of the size of the representative volume element for random composites: statistical and numerical approach. Int J Solid Struct 2003;40(13–14):3647–79.